Journal of Industrial and Engineering Chemistry 58 (2018) 328–333

Contents lists available at ScienceDirect

Journal of Industrial and Engineering Chemistry

journal homepage: www.elsevier.com/locate/jiec

Band structure of amorphous zinc tin oxide thin films deposited by atomic layer deposition

Sunyoung Lee[1], Sungjoon Kim[1], Seokhee Shin, Zhenyu Jin, Yo-Sep Min*

Department of Chemical Engineering, Konkuk University, 120 Neungdong-Ro, Gwangjin-Gu, Seoul 05029, Republic of Korea

ARTICLE INFO

Article history:
Received 17 August 2017
Received in revised form 23 September 2017
Accepted 24 September 2017
Available online 4 October 2017

Keywords:
Zinc tin oxide
Band structure
Atomic layer deposition
Work function
Buffer layer

ABSTRACT

Recently, zinc tin oxide (ZTO) has attracted attention as an alternative buffer layer to replace CdS for photovoltaic cells. ZTO thin films were grown by atomic layer deposition from diethylzinc, tetrakis (dimethylamido)tin, and water. Compositional, structural and optical properties were characterized to construct band diagram of the ZTO films depending on Sn content. The ZTO films exhibit optical bandgaps of 2.95–3.07 eV which are wider than that of CdS. Furthermore, their work function is also observed to vary in a wide range of 4.32–5.16 eV. It is attributed to incorporation of Sn into ZTO which strongly influences formation of oxygen vacancies.

Introduction

Thin-film photovoltaic (PV) cells directly and efficiently convert solar energy into electrical energy with the highest conversion efficiency of 22.6%, which has been observed for $Cu(In,Ga)Se_2$ (CIGS) solar cells [1]. Generally, thin-film PV cells such as CIGS solar cells require a buffer layer in their window layer stack to prevent unfavorable conduction band alignment that promotes interface recombination.

Commonly, *n*-type CdS is used as a buffer layer to sufficiently line up the conduction bands of chalcopyrite-type absorbers (e.g., CIGS, $CuGaSe_2$, $CuInSe_2$, or $Cu(In,Ga)(S,Se)_2$) and transparent ZnO in order to achieve high efficiency [2–4]. However, the disadvantages of using CdS as a buffer layer significantly overweigh its advantages. The CdS is usually prepared by non-vacuum chemical bath deposition, whereas CIGS absorbers are commonly grown under vacuum (e.g., by co-evaporation), and are air-sensitive. In addition to these differences, PV cells containing CdS buffer layers cannot be easily commercialized and produced on an industrial scale due to the toxicity of CdS and its relatively small bandgap (E_g = 2.42–2.45 eV), which results in absorption of the blue part in the solar spectrum by the CdS layer, not by the absorber layer. Hence, other buffer layer materials need to be developed to reduce the above optical loss and promote the industrial production of PV cells.

The extensive search for suitable buffer layer materials revealed that in thin-film solar cells, In_2S_3 and certain Cd-free Zn-based compounds (e.g., $ZnO_{1-x}S_x$, $Zn_{1-x}Mg_xO_y$, and $Zn_{1-x}Sn_xO_y$) prepared by atomic layer deposition (ALD) achieve high efficiencies comparable to that of CdS [4–8]. Notably, $Zn_{1-x}Sn_xO_y$ (ZTO) thin films grown by ALD showed high performance in CIGS cells, achieving conversion efficiencies of up to 18.0% [7].

The alignment of conduction band levels in the heterojunctions of a PV cell plays a significant role in reducing unnecessary recombination at junction interfaces. Recently, Kapilashrami et al. reported that hybridization between the oxygen and metal states of ZTO films gives rise to variation of conduction and valence band edges depending on the Sn content [9]. However, the work function of ZTO buffer layers has not been characterized in detail. Despite the conduction band offset being considered, the Fermi level of a buffer layer needs to be closely investigated, since an undesired barrier can be additionally created by band bending induced from Fermi level alignment at equilibrium. Meanwhile, in amorphous oxide semiconductors, oxygen vacancy formation is known to be closely related to the charge carrier generation [10]. Therefore, it is required to understand the correlation between oxygen vacancy and Fermi level of which position is varied by the carrier concentrations.

Here, we investigated compositional and structural characteristics of the ternary ZTO thin films grown by ALD by X-ray photoelectron spectroscopy (XPS) and X-ray diffraction (XRD). Their optical bandgaps and work functions were also studied to

* Corresponding author.
E-mail address: ysmin@konkuk.ac.kr (Y.-S. Min).
[1] These authors equally contributed to this work.

https://doi.org/10.1016/j.jiec.2017.09.045
1226-086X/

construct the band structures of the ZTO films, depending on the Sn content, by using UV-visible spectroscopy and Kelvin probe force microscopy (KPFM). In addition, by using the proposed band structure of the ZTO films, diode characteristics of *n*-ZnO/*p*-Si, *n*-SnO_2/*p*-Si and *n*-ZTO/*p*-Si heterojunction were interpreted for various Sn content.

Experimental

ZTO thin films were grown on boron-doped *p*-type Si (100) wafers with a resistivity of 10.0 Ω cm (LG Siltron, Inc.) at 150 °C in a laminar flow-type reactor (CN1 Co., Ltd.). Prior to the ALD process, the Si wafers were etched in dilute HF solution (1.63%) to clean and remove native SiO_2. For specimens to obtain optical bandgaps, the ZTO thin films were grown on polished quartz substrates (Hanjin Quartz). Tetrakis(dimethylamido)tin(IV) (TDMASn) and diethylzinc (DEZ) were used as Sn and Zn precursors (Nuri Tech Co.), and water was utilized as an oxygen precursor. Both DEZ (vapor pressure ~9.2 Torr at 15 °C [11]) and water were vaporized from external canisters into the reaction chamber at room temperature. However, due to the low vapor pressure (~0.04 Torr at 40 °C) of TDMASn [12], the canister of Sn precursor was heated to 50 °C, and N_2 (50 sccm, 99.999%) was used as a carrier gas. DEZ, TDMASn, and water vapors were introduced at feed rates of 1.3×10^{-4}, 3.2×10^{-5}, and 1.3×10^{-3} mol/s, respectively. Every precursor pulse was followed by N_2 purging at a flow rate of 400 sccm. All delivery lines were constantly maintained at 100 °C. The base pressure of the reaction chamber was less than 40 mTorr, and ALD was operated at a working pressure range of 300–600 mTorr.

Similarly to the ternary ALD processes described by Hultqvist et al. [6] and Mullings et al. [13], one ZTO supercycle consisted of several subcycles of ZnO and SnO_2 deposition. A typical ZnO deposition process was described by a sequence of DEZ-N_2-H_2O–N_2 pulses with lengths of 1-10-1-10 s. For optimizing the saturation time of the Sn precursor, SnO_2 deposition was performed using a sequence of TDMASn-N_2-H_2O-N_2 pulses with lengths of 1-10-2-30 s. The desired Sn and Zn contents of ZTO thin films were obtained by varying the corresponding fractions of ZnO and SnO_2 subcycles in the total number of subcycles. For example, in order to achieve the ALD-preset subcycle fraction [Sn/(Sn + Zn)] of ~0.4, one supercycle comprised three ZnO and two SnO_2 subcycles [2/(2 + 3) = 0.4].

The thickness of ZTO thin films was determined by spectroscopic ellipsometry (SE; MG-1000, NanoView Co., Ltd.). The incidence angle of polarized light in the SE was fixed at ~70°, and the energy of the incident light is ranged in 1.5–5.0 eV. XPS (PHI 5000 VersaProbe, Ulvac-PHI) utilizing monochromatic Al K_α emission was employed to characterize the elemental composition and chemical states of ZTO films, in which the C 1 s peak (284.8 eV) of the adventitious carbon was used as an internal reference for calibration. For cleaning the surface of specimens, Argon sputtering was performed for 10 s in the XPS chamber by bombarding Ar^+ ions (2 keV). X-ray diffraction (XRD; Philips X'pert Pro MRD) patterns were recorded at an incidence angle of 1.0° using Cu K_α emission. UV-visible spectroscopy (Mega900, scinco) was also performed to determine optical bandgaps of each film grown on quartz substrates. Surface potential measurements and topography were performed by kelvin prove force microscopy (KPFM; XE-100, Park systems) using a Au–Cr coated cantilever (NSC14–cr–au; tip height = 12–18 μm, tip radius ~35 nm, and resonant frequency of 142 Hz).

The electrical properties of ZTO thin films were characterized utilizing *n*-ZTO/*p*-Si heterojunction diodes with different Sn contents, in which the thickness of ZTO on Si was ~20 nm. Ohmic contacts were formed by thermal evaporation–deposition of Al and Au as top and bottom electrodes, respectively. The Al top electrode was deposited with a shadow mask with a circle area of $\sim 1.26 \times 10^{-3}$ cm^2. Current density–voltage (*J*–*V*) curves of the diodes were recorded using a semiconductor parameter analyzer (HP 4145B).

Results and discussion

Growth rate and structural characteristics

Fig. 1 shows the thicknesses of the grown films for a total of 100 subcycles (i.e., 20 supercycles and 5 subcycles in each supercycle) as a function of the ALD-preset subcycle fraction of Sn/(Sn + Zn). The growth rates of ZnO [Sn/(Sn + Zn) = 0] and SnO_2 [Sn/(Sn + Zn) = 1] at 150 °C are 1.80 and 0.82 Å/cycle, respectively, which are well consistent with those reported by Mullings et al. [13]. However, ZTO thin films are grown far slower than expected from the growth rates of ZnO and SnO_2 considering the ALD-preset subcycle fraction (for the nominally-predicted thickness, see the dashed line). The retardation of ZTO growth can be explained by slow nucleation [14] and the incomplete removal of precursor-bound ligands [15].

Fig. 2 shows the XRD patterns of ALD-grown thin films. The ZnO film exhibits three distinct peaks attributed to (100), (002), and (101) planes, which reveal a hexagonal wurtzite-type polycrystalline structure. In contrast, the SnO_2 and ZTO thin films are amorphous, not showing any noticeable peaks.

Topographical images (Fig. S1) also show that ZnO thin film has a higher root-mean-squared (rms) surface roughness (0.82 nm) than those (0.35–0.50 nm) of SnO_2 and ZTO thin films, owing to the amorphous nature, except for the ZTO film with 52% Sn content. Even though the film of 52% Sn is also amorphous in XRD, it shows much higher roughness (2.98 nm) indicating the presence of plateau-like surface structure with a size of ~300 nm. It may be attributed to atomic migration for phase separation of ZTO due to thermodynamic instability. Recently, Heo et al. also observed the phase separation in ALD-ZTO films, and their particle size was around 300 nm. The phase separation occurs at an annealing temperature lower than the crystallization temperature [16]. It indicates that one phase of the ZTO film with comparable amounts of Zn and Sn is thermodynamically less stable than the separated phases (Zn-rich and Sn-rich phases). Indeed, the depth profile (Fig. S2) of the film reveals that the Sn content severely decreases in the direction of depth, but the Zn content increases in the same

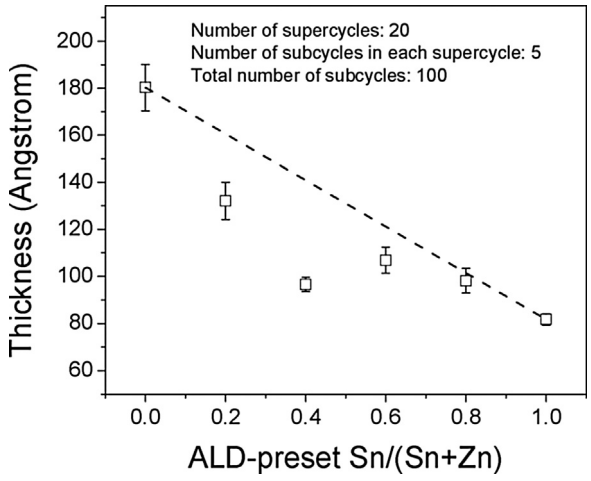

Fig. 1. Thickness of ZTO films as a function of the ALD-preset Sn/(Sn + Zn) subcycle fractions for a total of 100 subcycles at 150 °C. The dashed line indicates ZTO thickness expected from the growth rates of ZnO and SnO_2 growth.

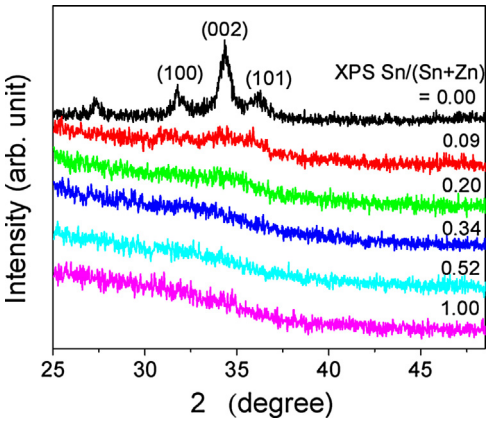

Fig. 2. XRD patterns of the grown films with different Sn/(Sn + Zn) fractions determined by XPS. All films were deposited at 150 °C and had a thickness of ~20 nm.

direction as a result of the atomic migration (upward for Sn and downward for Zn atoms).

Work functions, bandgaps and oxygen vacancies

True Sn/(Sn + Zn) ratios in ternary oxide films were determined by XPS analyses. In order to avoid over- or under-estimation of the ratio, the compositional analyses were performed twice for each specimen before and after cleaning the surface. For cleaning the adventitious C atoms on the sample surface, Ar^+ ions were bombarded with an energy of 2 keV for 10 s. Fig. 3(a) illustrates correlation between XPS-determined Sn/(Sn + Zn) and the ALD-preset Sn/(Sn + Zn). If the Sn content linearly increases with the nominal ALD-preset subcycle fraction, the true contents of Sn should be plotted as indicated with dashed line. However, the true Sn/(Sn + Zn) ratios are smaller than those in the dashed line. This result may attribute to the slow growth rates of SnO_2. Similar results were also reported by other groups by using inductively-coupled plasma optical emission spectroscopy [13] and Rutherford backscattering spectrometry [7]. However, as shown in Fig. S3, the Sn/(Sn + Zn) ratio is overestimated on the ZTO films without Ar^+ bombardment, because of the ultrathin detection depth of XPS and the presence of the adventitious contaminants.

Fig. 3(b) shows variation of oxygen content [O/(Sn + Zn)] as a function of the ALD-preset Sn/(Sn + Zn). There are large differences between before- and after-cleaning specimens for all ZnO, SnO_2 and ZTO films. The oxygen content may be overestimated for the before-cleaning specimens due to the presence of oxygen in the adventitious carbon compounds and surface-adsorbed H_2O, but underestimated for the after-cleaning specimens by preferential sputtering of oxygen atoms. It was already reported that the oxygen atoms are preferentially sputtered from ALD-grown ZnO film [17]. Therefore, the real ratio of oxygen to metal atoms may locate between the values of before and after cleaning.

The influence of Sn incorporation on the chemical states of ZTO films was investigated by deconvoluting their O 1s spectra into three peaks at 531.3 eV (lattice oxygen, O_L), 532.61 eV (oxygen nearby oxygen-deficient ZTO, O_V), and 533.47 eV (oxygen in water molecules adsorbed on ZTO surface, O_{OH}) [18,19]. Fig. 3(c)–(f) shows that the oxygen deficiency in the ZTO is closely correlated to Sn content. With increasing Sn content, the relative area of the O_V peak decreases from 0.30 (9% Sn in ZTO) to 0.18 (52% Sn in ZTO) as shown in Fig. S4(c). According to Liu et al., the ionic potential, which is defined as an ion's charge divided by its radius, of Sn^{4+} (5.63/Å) is much higher than that of Zn^{2+} (2.70/Å) [19,20]. The strength of the Sn–O bond (528 kJ/mol) is much stronger than that of the Zn–O bond (<250 kJ/mol) [21]. For these reasons, the incorporation of Sn may inhibit the formation of oxygen vacancies in ZTO thin films during ALD. Jeong et al. reported that during oxygen vacancy formation, lattice oxygens decompose into oxygen gas (O_2), a doubly charged oxygen vacancy, and two free electrons [10]. Thus, it can be presumed that charge carrier generation in ZTO

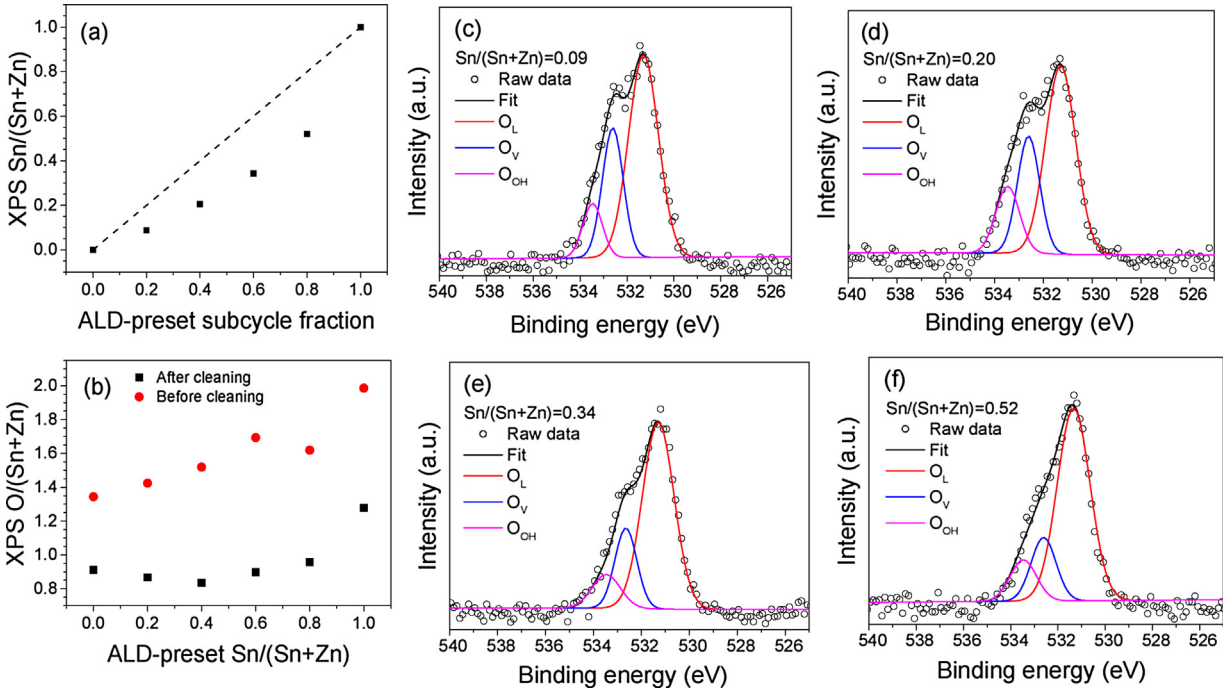

Fig. 3. (a) Correlation between XPS-determined and ALD-preset Sn/(Sn + Zn) ratios, (b) correlation between the XPS-determined O/(Sn + Zn) ratio and the ALD-preset Sn/(Sn + Zn) ratio. O 1s spectra of ZTO films with Sn contents of (c) 9%, (d) 20%, (e) 34%, and (f) 52%. All samples were deposited at 150 °C and had a thickness of ~20 nm.

is more severely hindered as the Sn content increases due to the decrease of oxygen vacancies.

Absorption coefficients (α) of ALD-ZTO with different Sn contents were determined with ~20-nm-thick ZTO films on quartz substrates in a spectral range of 1.37–6.20 eV by UV-visible spectroscopy using the Beer–Lambert law ($A = \alpha t$ where A and t are absorbance and thickness). The optical bandgaps of amorphous semiconductors are often characterized from the intercept on the abscissa of the Tauc plot in which the value of $(\alpha h\nu)^r$ is plotted against the value of photon energy ($h\nu$) [22,23]. The values of the exponent (r) are different depending on the nature of the transition: $r = 2$ for direct allowed transitions and $r = 1/2$ for indirect allowed transitions. Generally, the optical absorption spectrum of amorphous semiconductor resembles that of the indirect transition in its crystalline phase, even though the spectrum has a tail due to localized states at lower energies than the bandgap. Fig. 4 shows the variation of bandgaps of the ALD-grown films depending on the Sn content, where the square and circular symbols indicate the bandgaps obtained under the assumptions of $r = 2$ and $r = 1/2$, respectively. As shown in Fig. 2, since the films of ZTO and SnO_2 grown at 150 °C are amorphous, they were fitted under the assumption of the indirect transition ($r = 1/2$). However, ZnO film was fitted with $r = 2$, because it is polycrystalline. See Fig. S5 for the Tauc plots of each film.

The optical bandgap (square symbol) of ZnO grown at 150 °C is evaluated to be ~3.28 eV, being in good agreement with previously reported value [9]. Even though polycrystalline SnO_2 has a direct bandgap of 3.6–4.0 eV [24], the amorphous SnO_x by ALD exhibits much smaller bandgap (2.36 eV) possibly, due to the oxygen deficiency in the non-stoichiometric SnO_x ($x < 2$). Recently, other groups also reported similar bandgaps of SnO_x films grown by ALD by using spectroscopic ellipsometry (2.9 eV) or soft X-ray spectroscopy (2.2 eV) [9,13]. In Fig. 4, the symbols of × and + indicate the values of bandgaps determined by SE and soft X-ray spectroscopy, respectively [9,13]. The amorphous ZTO films exhibits small variation in the range of 2.95–3.07 eV in this work. However, depending on the analytical methods, the bandgaps of ZTO are scattered even in a similar composition. Nonetheless, the overall trend is that the bandgaps of ZTO approximately locates between those of ZnO and SnO_x, regardless of the methods. In addition, ZTO and SnO_x films exhibit significant tails in their UV-visible spectra (Fig. S5) which are attributed to the subgap absorptions due to the presence of localized states in the bandgaps. Meanwhile, the tail of the polycrystalline ZnO film is relatively negligible. According to the recent DFT calculation [25], the conduction and valence bands of amorphous oxide semiconductors are mainly formed by density of states (DOS) originated to metal s-state and oxygen $2p$-state, respectively. Especially, the valence band shows strong band tailing due to the p-like character of O $2p$ states.

To construct the band diagram of ZTO thin films, their work functions were measured by KPFM under ambient conditions (Fig. 5). In the KPFM, a surface potential offset between a sample and the probe tip, due to their work function difference, can be measured by using a null circuit to drive a DC voltage on the tip to a value which minimizes the vibration of the cantilever. The value of the DC voltage at the minimal vibration corresponds to contact potential difference (V_{CPD}). By measuring V_{CPD}, the work function (φ_{sample}) of the sample can be determined by the equation: $V_{CPD} = (\varphi_{tip} - \varphi_{sample})/q$ where φ_{tip} and q are the work function of the probe tip and elementary charge, respectively. For calibration of the work function of the probe tip, a highly ordered pyrolytic graphite (HOPG) was used as a reference material ($\varphi_{HOPG} = 4.65$ eV), since it is well known that HOPG does not form interface dipole even in ambient air [26]. All films were measured on three different positions of the sample surface.

In Fig. 5, the work function of ZnO grown at 150 °C was measured to be 4.65 eV which agrees to the value of 4.65 eV evaluated from n-ZnO/p-Si, prepared at 175 °C by ALD, using Schottky–Mott model [27]. The work function of SnO_2 is observed to be 4.49 eV. This value also agrees with those (4.25–4.48 eV) of sputtered SnO_2 thin films which are measured by ultraviolet photoelectron spectroscopy [28]. For the ZTO films, the work function (φ_{ZTO}) significantly varies depending on the Sn content. The value of φ_{ZTO} reaches a maximum of 5.16 ± 0.04 eV at 34% Sn. Before reaching the maximum work function, the φ_{ZTO} increases as the Sn content increases. Therefore, the Fermi energy level (E_F) of ZTO decreases in the Sn content range of 0–34%. Consequently, charge carrier density of ZTO may be reduced as the Sn content increases in the range. Intriguingly, the φ_{ZTO} is smallest (4.32 ± 0.05 eV) at 52% Sn, even though the Sn content is highest among the specimens. The KPFM surface potential image (Fig. S1 (h)) of the 52% Sn ZTO does not show significant variation over the surface, although the AFM image (obtained at the same region) reveals the high roughness. This may be mainly attributed to the atomic migration (Sn upward and Zn downward) mentioned in the above section. Note that the workfunctions of the Zn-rich and Sn-rich regions may resemble those of ZnO (4.65 eV) and SnO_2

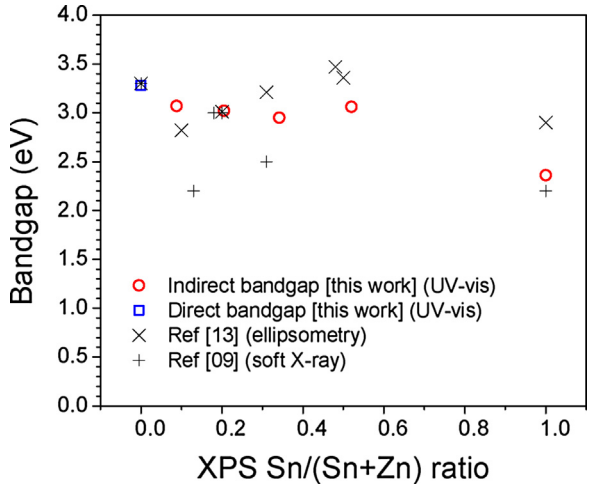

Fig. 4. Directly (black squares) and indirectly (red circles) Tauc-fitted bandgaps of ZTO determined by UV-Vis spectroscopy. All samples were deposited on quartz plates at 150 °C and had a thickness of ~20 nm.

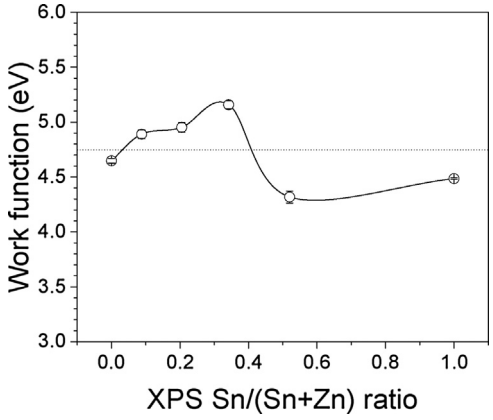

Fig. 5. Work function difference of ZnO, ZTO and SnO_x films determined by KPFM depending on XPS Sn/(Sn + Zn) ratio. All samples were deposited at ~20 nm-thick on Si wafers with 300-nm thick SiO_2 at 150 °C. The horizontal dotted line indicates the work function (4.74 eV) of boron-doped p-Si wafer (10.0 Ω cm) which is used to fabricate ZTO/Si diodes.

Table 1
Bandgaps, electron affinities, and work functions of ALD-prepared ZTO films.

XPS Sn/(Sn+Zn) ratio	E_g (eV) [this work]	E_g (eV) [12]	χ (eV) [12]	Φ (eV) [this work]	E_C–E_F (eV)
0	3.28	3.3	4.35	4.65	0.30
0.09	3.07	–	–	4.89	–
0.13	–	2.2	4.25	–	–
0.18	–	3.0	4.15	–	–
0.21(0.20)	3.02	3.0	4.05	4.95	0.90
0.34(0.31)	2.95	2.5	4.25	5.16	0.91
0.52	3.06	–	–	4.32	–
1	2.36	2.2	4.45	4.49	0.04

(4.49 eV), respectively. The variation of the potential over the surface of the 52% Sn ZTO is not noticeable owing to the small difference in workfunctions between ZnO and SnO_2. In addition, the overall trend of work function in Fig. 5 is in good agreement with that in a previous study, wherein the work function of solution-processed ZTO was investigated with its Sn content [29].

Hall measurements, generally performed to determine charge carrier density, could not be applied to ALD-deposited ZTO films, since these films exhibit overly high resistivity due to the poor conductivity of SnO_2 [30]. Although the charge carrier concentration of ZTO is hard to determine directly, it can be roughly estimated from the energy difference (E_C–E_F) between conduction band edge and Fermi level.

Band diagrams and heterojunctions

Table 1 summarizes the bandgaps (E_g) and work functions determined in this study. Kapilashrami et al. reported that the bandgaps and electron affinities (χ) of ZTO films by using soft X-ray emission and absorption spectroscopy as also listed in Table 1 [9]. By using the values of E_g, φ, and χ, the values of E_C–E_F were calculated to construct the band diagrams of ZnO, SnO_2, and ZTO grown at 150 °C by ALD.

In Fig. 6, the representative band diagrams of ZTO films (21% Sn and 34% Sn) are compared with those of ZnO and SnO_2 films. In order to confirm the validity of the band diagrams, we fabricated *n*-ZnO/*p*-Si, *n*-SnO_2/*p*-Si and *n*-ZTO/*p*-Si heterojunction diodes and examined their current density–voltage (*J*–*V*) characteristics (Fig. 7). All diodes clearly show the rectifying behavior in which *J* exponentially increases as the forward bias (negative voltage applied on *n*-type thin film) increases. However, the magnitudes of *J* at a forward bias (e.g. *V* = −2 V) are largely different depending on the Sn content. To compare the rectifying behaviors, we added equilibrium energy band diagrams of each diode in Fig. S6.

For the *n*-ZnO/*p*-Si and *n*-SnO_2/*p*-Si diodes, it is expected that ZnO may have lower majority carrier concentration than SnO_2, according to the values of E_C–E_F (0.30 eV for ZnO and 0.04 eV for SnO_2). However, the former shows more clear rectifying behavior than the latter, because the energy barrier (0.39 eV) overcome by majority carrier of ZnO is smaller than that (0.65 eV) of SnO_2 (Fig. S6). In addition, it is expected that the higher mobility of polycrystalline ZnO also contributes to the higher *J* values, because the mobility is severely influenced by the crystallinity, noting that SnO_2 is amorphous.

Unlike the ZnO and SnO_2, the charge carrier concentrations of both ZTO films are much lower than those of ZnO and SnO_2, due to a large value of E_C–E_F (0.90 eV for 21% Sn and 0.91 eV for 34% Sn ZTO). Thus, in case of ZTO diodes, the charge carriers (holes) of *p*-Si have a dominant effect on the forward current flow, rather than electrons of *n*-ZTO. As can be seen in Fig. S6, holes of the *p*-Si side in ZTO diodes has a large barrier height (~1.8 eV for both ZTO diodes). In other words, the forward bias allows holes to have sufficient energy to surmount the potential barrier, which causes that the forward current in ZTO diodes goes up exponentially with applied voltage, showing a rectifying characteristic.

Fig. 7 reveals that the forward current density of 34% Sn ZTO is much lower than that of 21% Sn ZTO. This is explained by the fact that the addition of Sn in ZTO films leads to a decrease of the mobility [16]. It means that the majority carriers are more difficult to flow through 34% Sn ZTO than 21% Sn ZTO, due to more severe scattering. Moreover, the positive conduction band offset of 0.2 eV in the 34% Sn ZTO, which is given by the difference in electron affinity of each semiconductor, causes an additional barrier for electrons to overcome. Meanwhile, the 21% Sn ZTO diode exhibits barrier-free conduction band alignment for electrons.

The reverse current density under reverse biases is shown in Fig. 7 (inset). When the diode is reversely biased (i.e., positive voltage applied on the *n*-type thin film), the reverse current

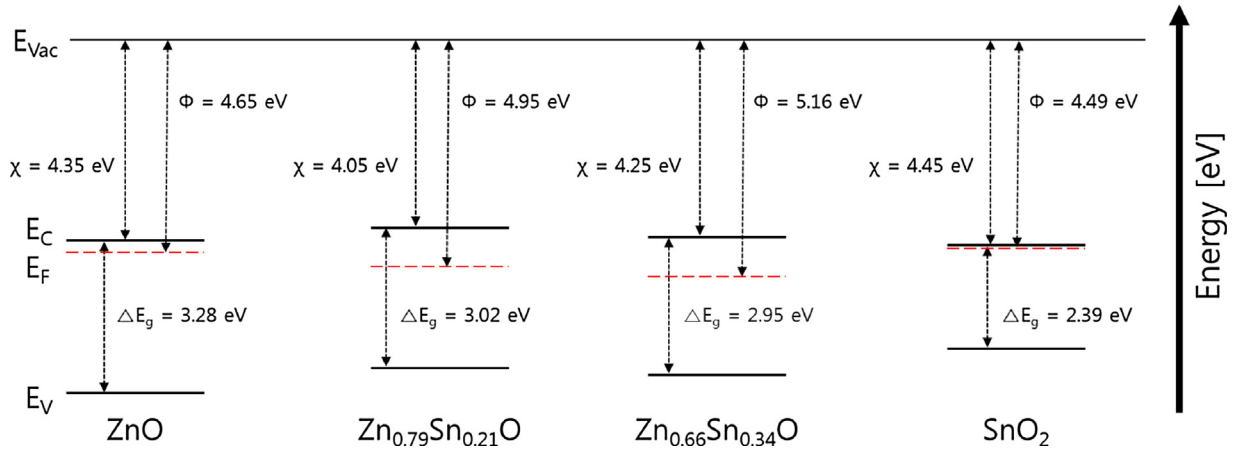

Fig. 6. Band diagrams of ZnO, 21% Sn-ZTO, 34% Sn-ZTO, and SnO_2.

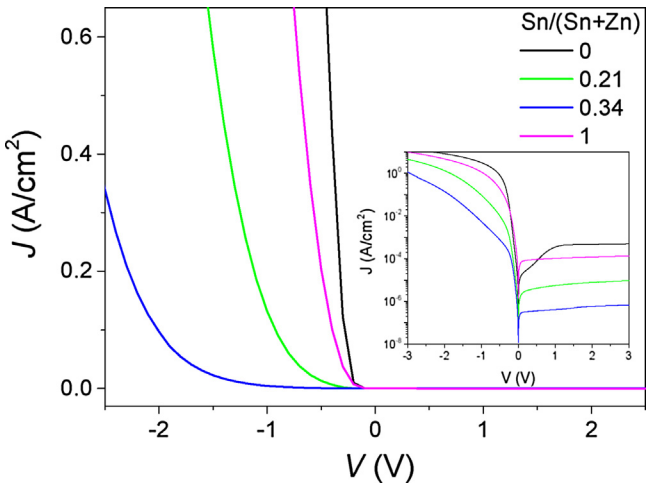

Fig. 7. Current density–voltage (J–V) curves of n-ZTO/p-Si heterojunctions with different Sn and Zn contents. Inset shows semi-log current density–voltage (log J–V) curves to clearly exhibit reverse current characteristics.

associates with the flow of minority carriers in the depletion region. Unlike the ideal diode, indirect thermal generation process significantly influences on the reverse current of real diodes fabricated with non-crystalline materials, owing to high defect concentrations [31]. The high carrier concentrations of ZnO or SnO_2 results in a wide depletion in the p-Si side. However, ZTO films, of which the values of E_C–E_F are much larger than ZnO or SnO_2 films, give rise to a narrow depletion in the p-Si side. Therefore, the indirect thermal generation in n-ZnO/p-Si or n-SnO_2/p-Si diodes readily occurs to increase the reverse current than in n-ZTO/p-Si diodes, due to the wider depletion width. Consequently, the reverse current densities of n-ZnO/p-Si or n-SnO_2/p-Si diodes are higher than those of ZTO diodes.

In addition, the reverse current in the n-ZnO/p-Si diode is slightly higher than that of n-SnO_2/p-Si diode. It can be explained with the difference in mobility of polycrystalline-ZnO and amorphous-SnO_2. Similarly, because the mobility of 34% Sn ZTO is lower than that of 21% Sn ZTO [16], minority carriers in the 34% Sn ZTO diode are also hard to transport under reverse bias, as majority carriers at forward bias did. In overall, the same trend of current density are observed under both reverse and forward biases.

Conclusions

We have grown ZnO, SnO_2, ZTO thin films with various Sn contents at 150 °C by ALD. Their compositional, structural and optical properties were investigated to construct the comprehensive band diagrams of ZTO films depending on the Sn content. It is demonstrated that the incorporation of Sn into ZTO films hinders the generation of oxygen vacancies. Consequently, work functions of ZTO could be engineered by adjusting the Sn contents, since the Fermi level, influenced by carrier concentration, was varied by the amount of oxygen vacancies. In order to confirm the validity of the constructed band diagrams, the diode characteristics of heterojunctions were also investigated for n-ZnO/p-Si, n-SnO_2/p-Si and n-ZTO/p-Si. According to the equilibrium energy band diagrams of each diode, it is clearly shown that the barrier height overcome by charge carriers is contributed by not only conduction band offset, but also band bending induced by the work function difference in the heterojunction. Especially, the band diagram of the ALD-ZTO films will be useful to understand the band alignment of a PV cell with a buffer layer of ZTO film such as CIGS solar cells.

Acknowledgments

This work was supported by Basic Science Research Program through the National Research Foundation of Korea (NRF: 2014R1A1A2055812). This research was also partially supported by the Korea Institute of Energy Technology Evaluation and Planning (KETEP: 20153030013060) and the Korea Evaluation Institute of Industrial Technology (KEIT: 10063277).

Appendix A. Supplementary data

Supplementary data associated with this article can be found, in the online version, at https://doi.org/10.1016/j.jiec.2017.09.045.

References

[1] P. Jackson, R. Wuerz, D. Hariskos, E. Lotter, W. Witte, M. Powalla, Phys. Status Solidi — Rapid Res. Lett. 10 (8) (2016) 583.
[2] R. Caballero, et al., J. Phys. Condens. Matter 19 (2007) 356222.
[3] S.N. Qiu, W.W. Lam, C.X. Qiu, I. Shih, Appl. Surf. Sci. 113/114 (1997) 764.
[4] P. Arnou, et al., Thin Solid Films 633 (2017) 76.
[5] N. Naghavi, et al., Prog. Photovolt. Res. Appl. 18 (2010) 411.
[6] Adam Hultqvist, Charlotte Platzer-Björkman, Uwe Zimmermann, Marika Edoff, Tobias Törndahl, Prog. Photovolt. Res. Appl. 20 (2012) 883.
[7] J. Lindahl, J.T. Wätjen, A. Hultqvist, T. Ericson, M. Edoff, T. Törndahl, Prog. Photovolt. Res. Appl. 21 (2013) 1588.
[8] N. Naghavi, S. Spiering, M. Powalla, B. Canava, A. Taisne, J.-F. Guillemoles, S. Taunier, A. Etcheberry, D. Lincot, Mater. Res. Soc. Symp. Proc. 763 (2003) B9.9.1.
[9] M. Kapilashrami, et al., Phys. Chem. Chem. Phys. 14 (2012) 10154.
[10] S. Jeong, Y.G. Ha, J. Moon, A. Facchetti, T.J. Marks, Adv. Mater. 22 (12) (2010) 1346.
[11] H.Y. Lee, C.J. An, S.J. Piao, D.Y. Ahn, M.T. Kim, Y.S. Min, J. Phys. Chem. C 114 (43) (2010) 18601.
[12] J.W. Elam, D.A. Baker, A.J. Hryn, A.B.F. Martinson, M.J. Pellin, J.T. Hupp, J. Vac. Sci. Technol. A Vac. Surf. Film. 26 (2) (2008) 244.
[13] M.N. Mullings, C. Hägglund, J.T. Tanskanen, Y. Yee, S. Geyer, S.F. Bent, Thin Solid Films 556 (2014) 186.
[14] J.T. Tanskanen, C. Hagglund, S.F. Bent, Chem. Mater. 26 (2014) 2795.
[15] A.J.M. Mackus, C. Macisaac, W.H. Kim, S.F. Bent, J. Chem. Phys. 146 (2017) 52802.
[16] J. Heo, S.B. Kim, R.G. Gordon, Appl. Phys. Lett. 101 (11) (2012).
[17] Y.-S. Min, C.J. An, S.K. Kim, J. Song, C.S. Hwang, Bull. Korean Chem. Soc. 31 (9) (2010) 2503.
[18] B. Du Ahn, D.W. Choi, C. Choi, J.S. Park, Appl. Phys. Lett. 105 (2014) 92103.
[19] L.-C. Liu, J.-S. Chen, J.-S. Jeng, W.-Y. Chen, ECS J. Solid State Sci. Technol. 2 (4) (2013) Q59.
[20] C. Kittel, Introduction to Solid State Physics, Sixth ed., Wiley, New York, 1986.
[21] Y.-R. Luo, Comprehensive Handbook of Chemical Bond Energies, CRC Press, 2007.
[22] J. Tauc, Mater. Res. Bull. 3 (1) (1968) 37.
[23] J. Tauc, R. Grigorovici, A. Vancu, Phys. Status Solidi 15 (2) (1966) 627.
[24] M.N. Mullings, C. Hagglund, S.F. Bent, J. Vac. Sci. Technol. A 31 (6) (2013) 61503.
[25] J. Robertson, Phys. Status Solidi Basic Res. 245 (6) (2008) 1026.
[26] M. Lorenzoni, A. Giugni, B. Torre, Nanoscale Res. Lett. 8 (1) (2013) 1.
[27] V. Quemener, et al., J. Phys. D. Appl. Phys. 45 (2012) 315101.
[28] K. Rachut, C. Körber, J. Brötz, A. Klein, Phys. Status Solidi 8 (9) (2014).
[29] R.D. Chandra, et al., ACS Appl. Mater. Interfaces 6 (2) (2014) 773.
[30] D. Choi, W.J. Maeng, J.-S. Park, Appl. Surf. Sci. 313 (2014) 585.
[31] Robert F. Pierret, Semiconductor Device Fundamentals, Addison-Wesley, 1996.

Supporting Information

Band Structure of Amorphous Zinc Tin Oxide Thin Films Deposited by Atomic Layer Deposition

Sunyoung Lee,† Sungjoon Kim,† Seokhee Shin, Zhenyu Jin and Yo-Sep Min*

Department of Chemical Engineering, Konkuk University, 120 Neungdong-Ro, Gwangjin-Gu, Seoul 05029, Korea

*ysmin@konkuk.ac.kr

† These authors equally contributed to this work.

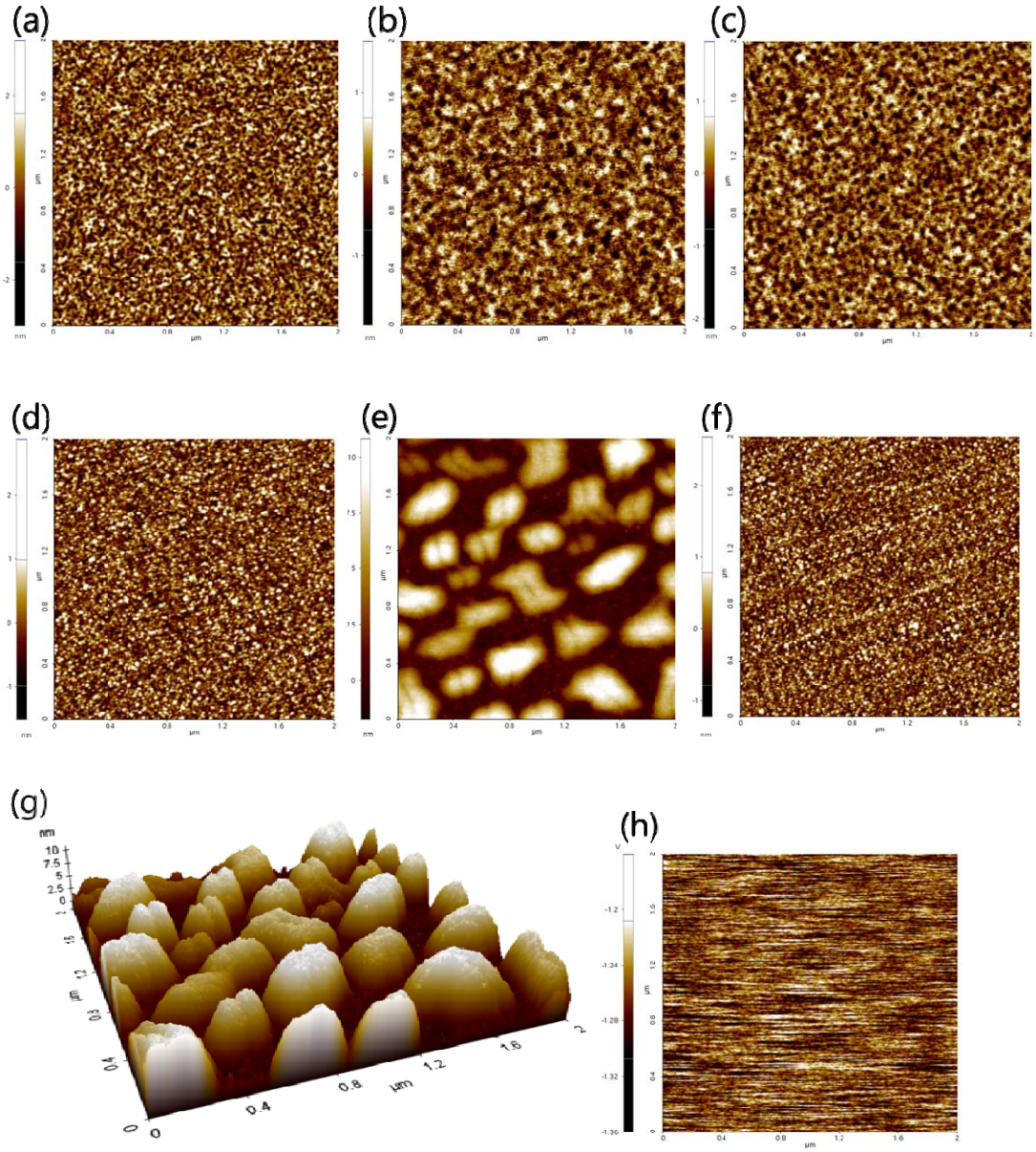

Figure S1. AFM images in an area of 2 × 2 μm^2. (a) ZnO (0.818 nm), (b) 9% Sn (0.351 nm), (c) 20% Sn (0.396 nm), (d) 34% Sn (0.502 nm), (e) 52% Sn (2.979 nm) in ZTO, and (f) SnO_2 (0.351 nm) deposited by ALD. The values in parenthesis are root-mean-square (rms) roughness. (g), (h) 3D image and KPFM image of 52% Sn ZTO in the same region in which the corresponding AFM image (e) was obtained.

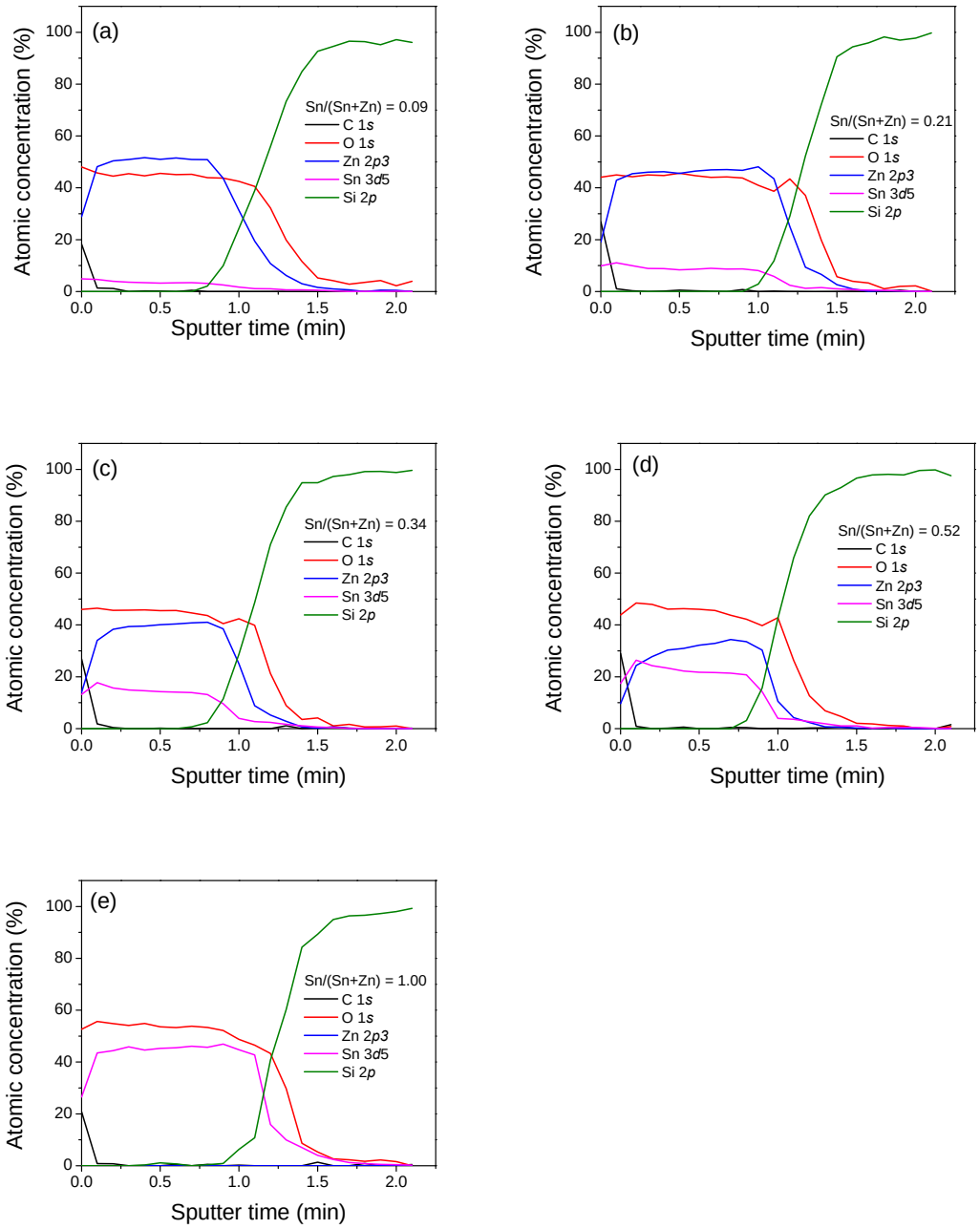

Figure S2. XPS depth profiles. (a) 9% Sn, (b) 20% Sn, (c) 34% Sn, (d) 52% Sn in ZTO, and (e) SnO_2 films.

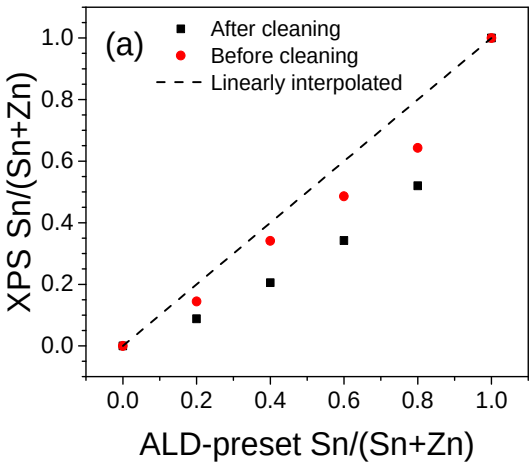

Figure S3. Comparison of XPS-determined Sn/(Sn + Zn) ratios of ZTO films before and after cleaning by Ar^+ bombardment.

There are small differences in the ratios of Sn/(Sn + Zn) estimated by XPS before and after cleaning the ZTO films. Two possible explanations can be suggested for the difference.

In XPS measurement, the distance that an electron can travel through matter without undergoing inelastic collisions is called the inelastic mean free path (IMFP). The IMFP of most elements is ranged in a few to dozens of angstroms [S1]. It should be noted that the ALD processes for ZTO growth were finished with the ALD sequence for SnO_2 at the final cycle of each ZTO process. Furthermore, there are adventitious contaminants on the surface before cleaning. Therefore, due to the nanometer-scale XPS detection depth and the presence of the contaminant on the topmost SnO_2 layer, the concentration of Sn in the ZTO without the Ar^+ bombardment may be overestimated.

The difference can be also influenced by different sensitivity factors of metal atoms in the bulk and on the surface. Generally, a constant sensitivity factor from a bulk state is used to quantitatively analyze the specimen in XPS experiment. However, the sensitivity factor can be varied depending on the chemical state of the element in the matrix. The value of sensitivity factor varies with the matrix because of the variability of the mean free path [S2]. Wanger et al. reported that the sensitivity factors for bulk cannot be applied to monolayer materials [S3], indicating that surface sensitivity factor is different from the bulk one for even same element.

Therefore, the real values of Sn/(Sn+Zn) of the ZTO films should be estimated after removing the adventitious contaminants.

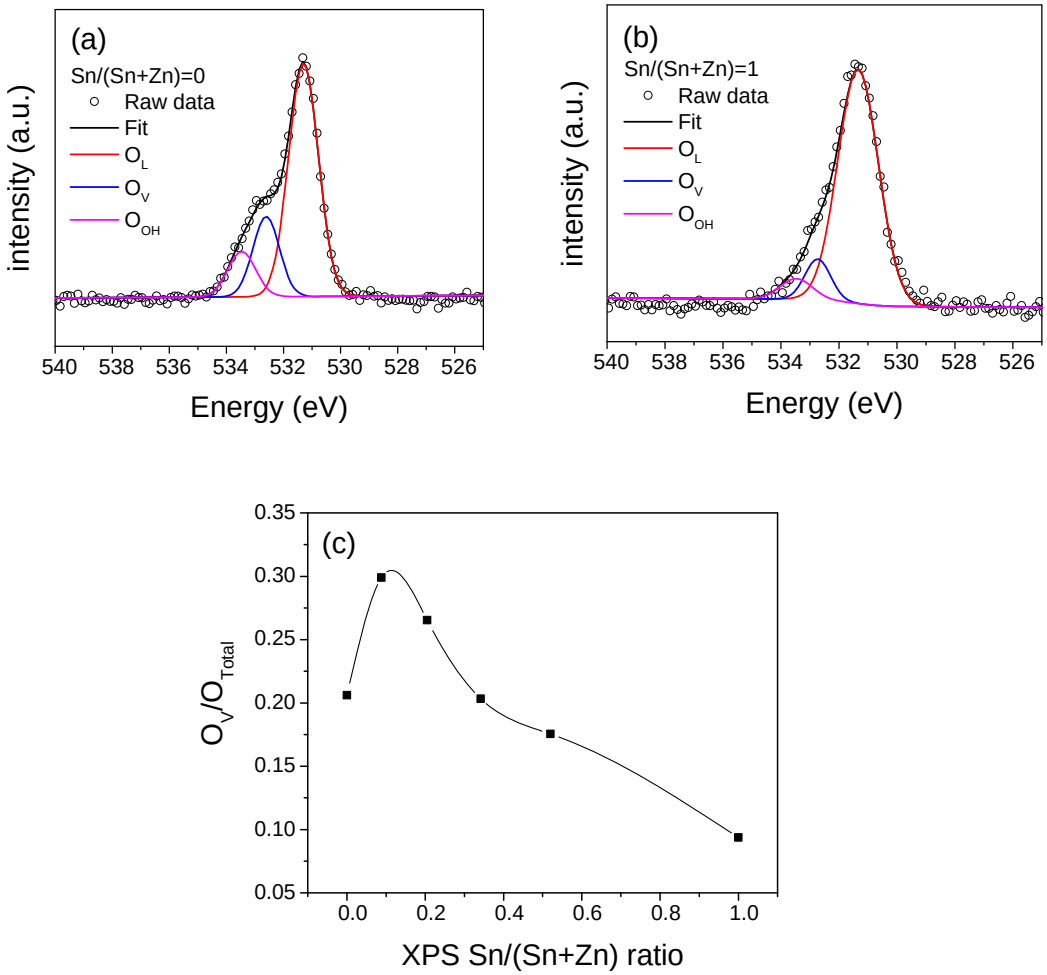

Figure S4. XPS spectra of O 1s of (a) ZnO and (b) SnO_2 film, and (c) ratio of oxygen vacancy to total oxygen as a function of XPS Sn/(Sn + Zn) ratio.

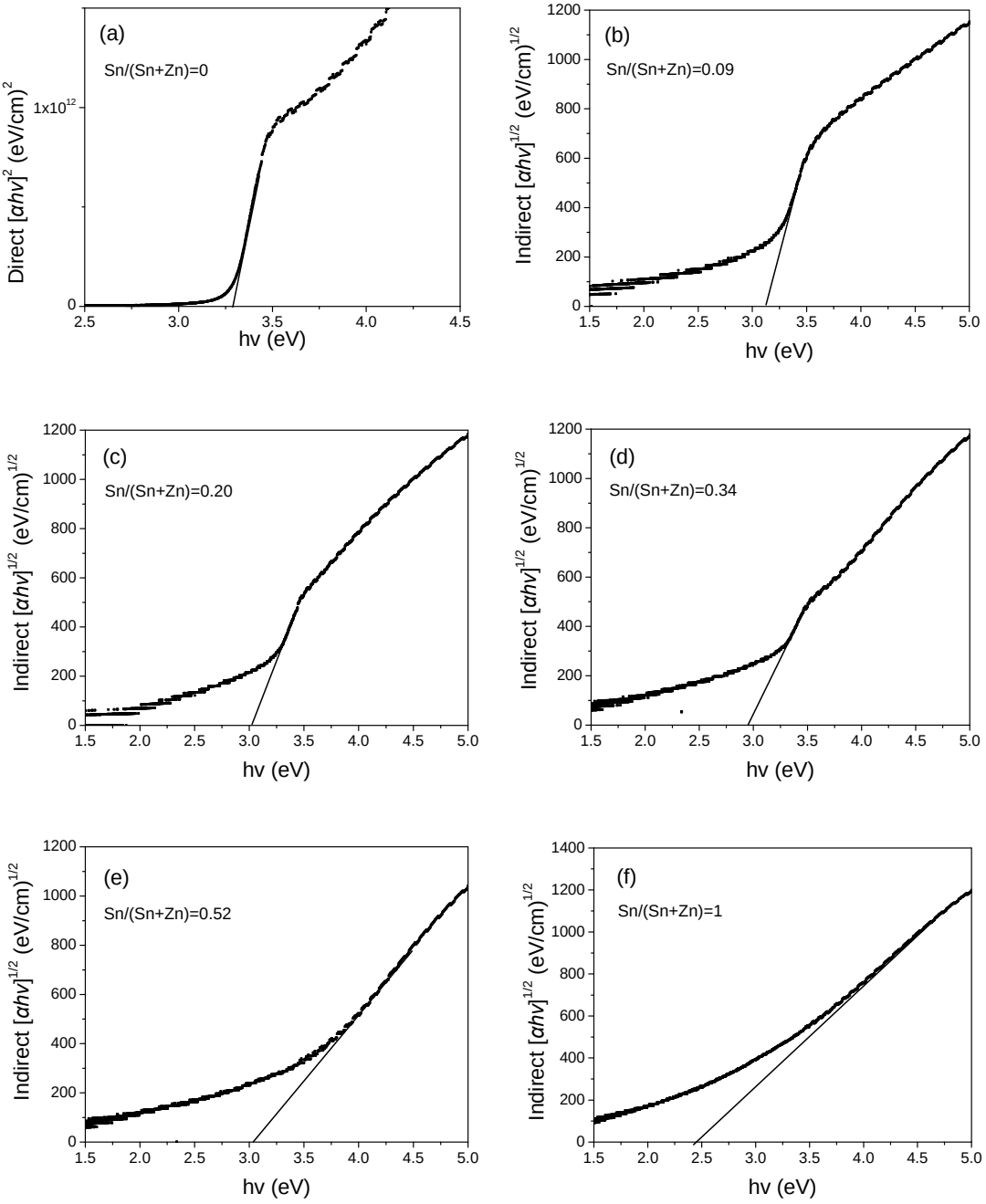

Figure S5. Tauc plots: (a) ZnO, (b) 9% Sn, (c) 20% Sn, (d) 34% Sn, (e) 52% Sn in ZTO, and (f) SnO_2 films.

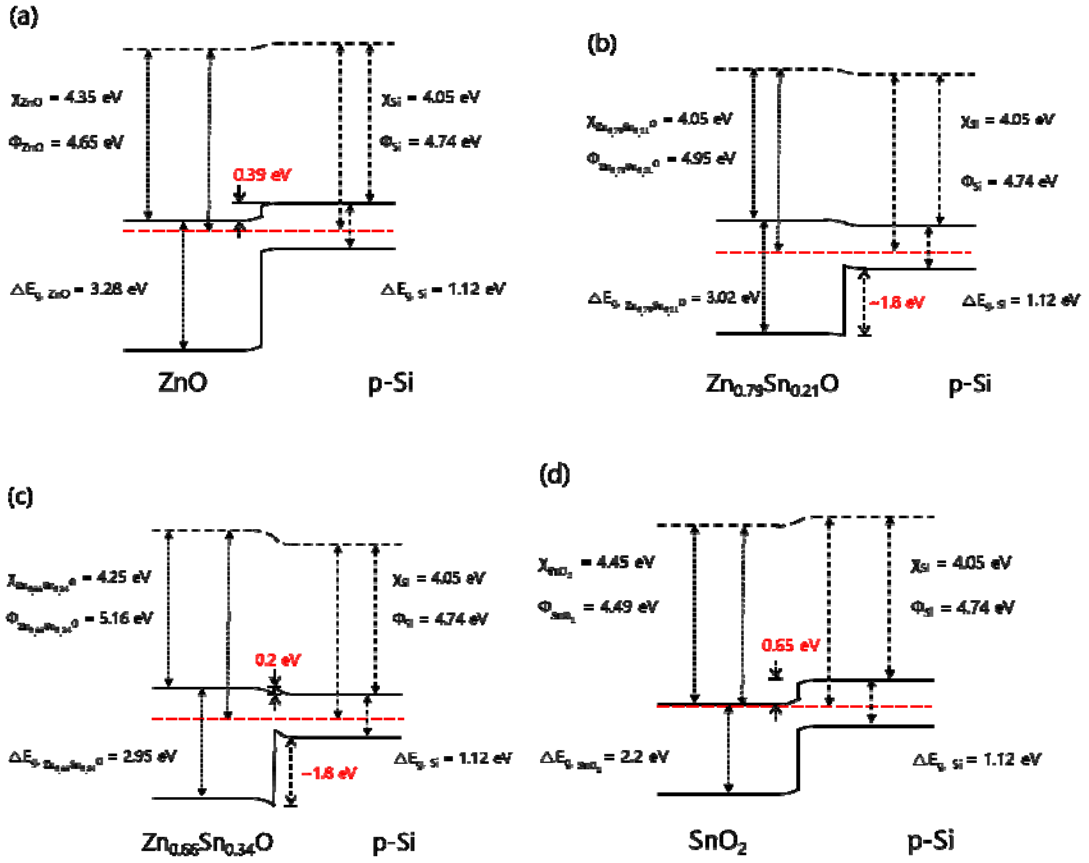

Figure S6. Equilibrium energy band diagrams of (a) *n*-ZnO/*p*-Si, (b) *n*-$Zn_{0.79}Sn_{0.21}O$/*p*-Si, (c) *n*-$Zn_{0.66}Sn_{0.34}O$/*p*-Si and (d) *n*-SnO_2/*p*-Si heterojunction.

References

[S1] John F. Watts and J. Wolstenholme, *An Introduction to Surface Analysis by XPS and AES*. 2003.

[S2] C. D. Wagner, L. E. Davis, M. V. Zeller, J. A. Taylor, R. H. Raymond, and L. H. Gale, "Empirical atomic sensitivity factors for quantitative analysis by electron spectroscopy for chemical analysis," *Surf. Interface Anal.*, vol. 3, no. 5, pp. 211–225, 1981.

[S3] C. D. Wagner, "Sensitivity factors for XPS analysis of surface atoms," *J. Electron Spectros. Relat. Phenomena*, vol. 32, no. 2, pp. 99–102, 1983.